Mineralium Deposita (2018) 53:1079–1094
https://doi.org/10.1007/s00126-018-0796-2

ARTICLE

Fluid evolution and ore genesis of the Dalingshang deposit, Dahutang W-Cu ore field, northern Jiangxi Province, South China

Ning-Jun Peng[1] · Shao-Yong Jiang[1] · Suo-Fei Xiong[1] · Dao-Hui Pi[1]

Received: 17 September 2017 / Accepted: 4 February 2018 / Published online: 15 February 2018

Abstract

The Dalingshang W-Cu deposit is located in the North section of the Dahutang ore field, northern Jiangxi Province, South China. Vein- and breccia-style tungsten-copper mineralization is genetically associated with Mesozoic S-type granitic rocks. Infrared and conventional microthermometric studies of both gangue and ore minerals show that the homogenization temperatures for primary fluid inclusions in wolframite (~ 340 °C) are similar to those in scheelite (~ 330 °C), but about 40 °C higher than those of apatite (~ 300 °C) and generally 70 °C higher than those in coexisting quartz (~ 270 °C). Laser Raman analysis identifies CH_4 and N_2 without CO_2 in fluid inclusions in scheelite and coexisting quartz, while fluid inclusions in quartz of the sulfide stage have variable CO_2 content. The ore-forming fluids overall are characterized by high- to medium-temperature, low-salinity, CH_4, N_2, and/or CO_2-bearing aqueous fluids. Chalcopyrite, muscovite, and sphalerite are the most abundant solids recognized in fluid inclusions from different ores. The H-O-S-Pb isotope compositions favor a dominantly magmatic origin for ores and fluids, while some depleted $\delta^{34}S$ values (− 14.4 to − 0.9‰) of sulfides from the sulfide stage are most likely produced by an increase of oxygen fugacity, possibly caused by inflow of oxidized meteoric waters. The microthermometric data also indicate that a simple cooling process formed early scheelite and wolframite. However, increasing involvement of meteoric waters and fluid mixing may trigger a successive deposition of base metal sulfides. Fluid-rock interaction was critical for scheelite mineralization as indicated by in-situ LA-ICP-MS analysis of trace elements in scheelite.

Keywords Fluid inclusion · Infrared microscopy · Scheelite · The Dalingshang W-Cu deposit · South China

Introduction

China has the most abundant tungsten resources in the world, which are mostly concentrated in the Nanling Range of central South China in southern Jiangxi Province and adjacent areas. However, in recent years, a cluster of W-Cu-rich deposits, such as the gaint Dahutang and Zhuxi deposits in northern Jiangxi Province, has been discovered on the northern margin of the Jiangnan Orogen in northeastern South China. The Dahutang ore field is among the largest ones in the region and perhaps in the world, with established resources of 2 Mt (million tonnes) WO_3, 0.65 Mt Cu, and 0.08 Mt Mo (Jiang et al. 2015), mainly in the Shimensi, Dalingshang, and Shiweidong deposits that are currently mined. Orebodies in these deposits are mainly of quartz vein, veinlet, and hydrothermal breccia style. In recent years, most research has been focused on mineral prospecting (Lin et al. 2006, 2006), geological features (Xiang et al. 2012, 2013; Jiang et al. 2015), geochronology, and geochemistry of ore-related granites (Huang and Jiang 2012, 2013, 2014; Mao et al. 2015), as well as molybdenite chronology and metal sources (Feng et al. 2012; Mao et al. 2013; Xiang et al. 2013). The consensus view of these studies is that the different W-Cu orebodies are temporally and genetically associated with the Mesozoic granitic rocks of crustal origin with emplacement ages of 150–130 Ma. However, origin and evolution of ore fluids have attracted much less attention in this district, and little systematic studies

Editorial handling: B. Lehmann

Electronic supplementary material The online version of this article (https://doi.org/10.1007/s00126-018-0796-2) contains supplementary material, which is available to authorized users.

✉ Shao-Yong Jiang
shyjiang@cug.edu.cn; shyjiang@nju.edu.cn

[1] State Key Laboratory of Geological Processes and Mineral Resources, Collaborative Innovation Center for Exploration of Strategic Mineral Resources and Faculty of Earth Resources, China University of Geosciences, Wuhan 430074, China

on fluid inclusions were carried out (Gong et al. 2015; Ye et al. 2017).

In this paper, the focus of study is on the Dalingshang deposit which occurs in the North section of the Dahutang ore field. Comprehensive studies of fluid inclusions in both ore minerals (wolframite and scheelite) and gangue minerals (apatite and quartz) were carried out using infrared and conventional microscopy. In addition, H-O isotopes of hydrothermal and igneous minerals, S-Pb isotopes of sulfide minerals, and in-situ LA-ICP-MS analyses of scheelite trace elements were obtained to constrain the source of the mineralizing fluids and to clarify the mechanisms of ore deposition.

Geological setting

The South China Block includes the Yangtze Craton in the west and the Cathaysia Block in the east, separated by the Qin-Hang suture (Fig. 1a). The Jiangnan Orogen lies near the boundary of the Yangtze Craton and Cathaysia Block, and is outlined by many Meso- to Neoproterozoic metasedimentary and igneous rocks (Fig. 1b) (Zheng et al. 2006). The Dahutang W-Cu ore field is located on the northern margin of the Jiangnan Orogen, consisting of the following deposits and prospects: the large-sized Shimensi and medium-sized Dalingshang ore deposits in the North section, the large-sized Shiweidong deposit in the South section, and many ore prospects in the Dawutang section, such as the Yikuangdai (No.1 ore belt), the Pingmiao, and Dongdouya areas (Fig. 1c).

The exposed strata of the Dahutang district include Quaternary sediments and the Neoproterozoic metasedimentary rocks of the Shuangqiaoshan Formation (Fig. 1c), which are mainly composed of siltstone, tuffaceous sandstone, shale, and phyllite slate intercalated with minor pyroclastic volcanic rocks (BGMRJX 1984). The Shuangqiaoshan Formation is dated at 824 ± 5 Ma (Gao et al. 2012) and exposed mainly in the southern part of the Dahutang area (Fig. 1c).

Intrusive rocks in the Dahutang district consist of Neoproterozoic granodiorite and various Mesozoic (Yanshanian) granites. The Neoproterozoic granodiorite is part of the Jiuling batholith, which is the largest granitoid complex in southeastern China with a total area of greater than 2300 km^2 (Xiang et al. 2013). The Mesozoic granitic intrusions were generated by multiple episodes of magmatism from 150 to 130 Ma (Lin et al. 2006; Jiang et al. 2015).

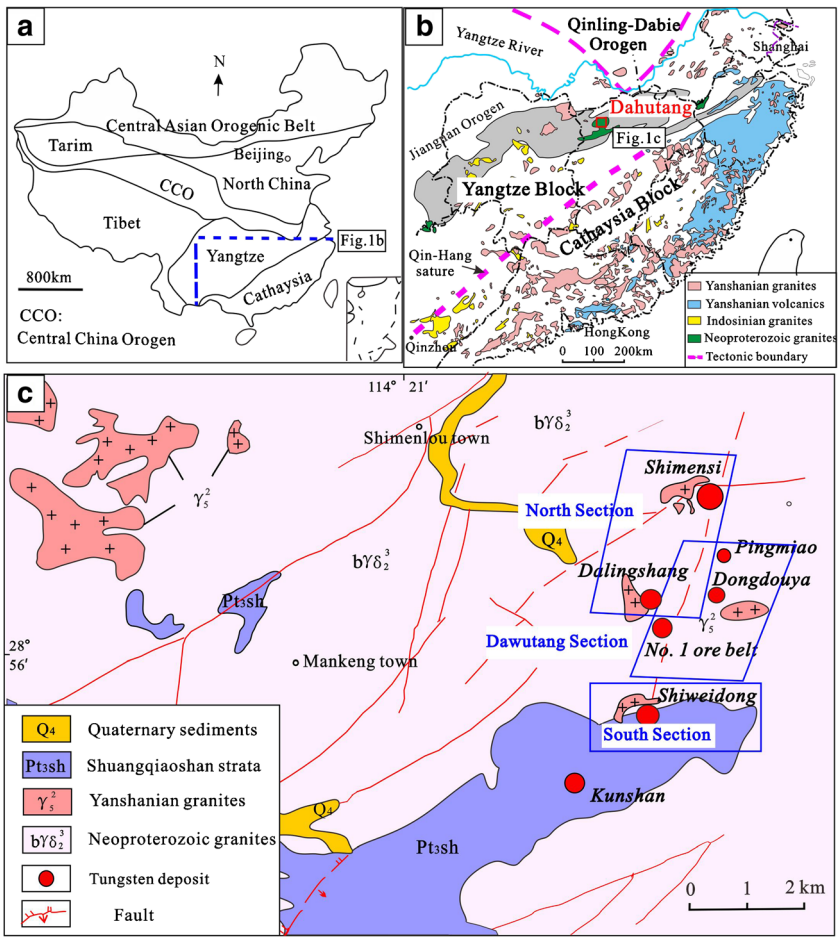

Fig. 1 **a** Tectonic map of China showing the main tectonic units and the Yangtze and Cathaysia blocks in South China. **b** Distribution of granites and volcanic rocks in South China, showing the location of the Dahutang W-Cu ore field (modified after Zhou et al. 2006). **c** Geological map of the Dahutang ore field, which is divided into three sections (North, South, and Dawutang). The main ore deposits include Shimensi, Dalingshang, Pingmiao, Dongdouya, Yikunagdai (No. 1 ore belt), Shiweidong, and Kunshan (modified after Xiang et al. 2013; Jiang et al. 2015)

Zircon U-Pb dating has bracketed their emplacement in two stages: (1) early stage (~ 144–150 Ma), porphyritic granitic rocks intruded in the Neoproterozoic batholith or in the Shuangqiaoshan strata, occurring as stocks or dikes; (2) late stage (130–135 Ma), middle- to fine-grained granites and granite porphyries cut through the early-stage Mesozoic granitoids or the Neoproterozoic batholith and occur as stocks, dikes, or sills. The Neoproterozoic granodiorite and all phases of Mesozoic granites are documented as silica-rich, strongly peraluminous, characterized by enrichment in Rb, U, and Pb, and depletion in Zr, Nb, Sr, and Ti. Integrated geochemical and Sr-Nd-Hf isotope studies have provided unambiguous evidence of an anatectic sedimentary origin for these granitoids (Huang and Jiang 2014; Jiang et al. 2015; Mao et al. 2015). Different orebodies are temporally and genetically associated with the Mesozoic intrusions and generally occur in their contact zones with the Neoproterozoic granodiorite.

The main geological structures of the Dahutang district include a series of EW- to NEE-, NE- to NNE-, NW-, and SW-trending faults (Fig. 1c). The EW-trending faults of Neoproterozoic age (Jinning period) and the NE- to NNE-trending faults of Mesozoic age (Yanshanian period) are two sets of the most important structures, spatially controlling not only the emplacement of the Mesozoic intrusions but also the distribution of ore deposits.

Ore deposit geology

The deposits in the Dahutang district have similar ore types, mineralogy, and paragenesis. The Dalingshang deposit of this study is under exploration, in which a prospecting tunnel (#81) is currently mined. This deposit contains a total of 18 orebodies and a total of 22,000 t WO_3, among which the orebodies III and V are the largest ones with WO_3 grade of 0.064–0.652% (average 0.140%) and 0.064–0.182 (average 0.130%), respectively (Jiang et al. 2015). Magmatic rocks include both Neoproterozoic and Mesozoic granitic intrusions. The Mesozoic granites have SHRIMP zircon U-Pb ages of 130–135 Ma (Huang and Jiang 2014), consisting mainly of medium- to fine-grained two-mica granite, fine-grained biotite granite, as well as many granite porphyry dykes (Figs. 2 and 3).

The Dalingshang deposit has various types of W-Cu mineralization: vein-type (including large quartz veins and small veinlets), hydrothermal breccia-type, and altered granite-type, among which the first type is of greatest importance, hosting > 95% of the total tungsten resource. The large quartz veins vary from 0.2 to 0.7 m in thickness and about 200 to 800 m in length. They dip steeply (70–85°) with a nearly EW strike, and always thin out or disappear at depth. The veinlets have a thickness between 1 and 30 mm and generally show disseminated, dendritic, or mesh structures. Both large veins and small veinlets are widely developed in the contact zones of Mesozoic granite with the Neoproterozoic granodiorite, especially in the altered exocontact zones. On the basis of crosscutting relationships, mineral assemblages, and textural observations, the paragenetic sequence has been recognized (Fig. 4), with the first stage being a pegmatite stage which occurs mostly as centimeter- to meter-wide pegmatite crust or shell on the top of the Mesozoic granite ("stockscheider"), followed by a silicate-oxide stage and a sulfide stage.

In the silicate-oxide stage, the ore-bearing quartz veins consist predominantly of quartz with some scheelite, wolframite, apatite, fluorite, and sulfides (Fig. 5; ESM Fig. 1). Wolframite and scheelite are the most abundant ore minerals. Wolframite commonly occurs in large veins as coarse crystals in tabular or columnar habit, locally as fine- to medium-grained crystals in groups or radiating aggregates (ESM Fig. 1a). In contrast, scheelite mostly occurs in veinlets as fine-grained anhedral crystal and is spatially associated with greisen selvages. Nevertheless, the two kinds of minerals are often found intergrown (Fig. 5a, b; ESM Fig. 1a–c). Both wolframite and scheelite are always distributed in the vein walls, indicating their deposition at an early stage of mineralization. Occasionally, apatite can be observed in coexistence with tungsten minerals (Fig. 5c). Pyrite is the first sulfide mineral after tungsten deposition, and is mostly replaced by chalcopyrite. Chalcopyrite is typically intergrown with bornite and may be cut by molybdenite, followed by the formation of tetrahedrite, enargite, chalcocite, stannite, pyrrhotite, and sphalerite. These sulfide minerals always replace early-formed wolframite, scheelite, and apatite (Fig. 5). Minor late-stage scheelite may occur as fillings of microfractures in quartz, locally crosscutting or replacing early-precipitated wolframite and chalcopyrite.

In the sulfide stage, quartz veins may contain appreciable chalcopyrite, and subordinate bornite, pyrite, molybdenite, tetrahedrite, enargite, and sphalerite, with minor wolframite and scheelite. Chalcopyrite, the dominant sulfide, occurs as anhedral masses intergrown with bornite in vein centers or as fillings of fractures in quartz at vein margins. For this stage, pyrite is classified in two types, with pyrite I replaced by chalcopyrite and later-formed pyrite II cutting chalcopyrite (Fig. 5j, k). Minor tetrahedrite and enargite commonly occur as inclusions or "disease" in chalcopyrite. Molybdenite is locally abundant and generally exhibits hexagonal crystal shape with a diameter of 2–20 mm. Scheelite formed as small irregular disseminations that crosscut massive chalcopyrite, indicating a later formation.

Hydrothermal alteration associated with vein-type ores is extensive, with greisenization being the major type, consisting mainly of quartz, muscovite, and minor apatite, fluorite, and biotite, accompanied by some wolframite, scheelite, and sulfide minerals (ESM Fig. 2). In general, biotite is altered to muscovite and plagioclase is intensely converted to sericite and quartz (ESM Fig. 2a, e). The metal content of the veins

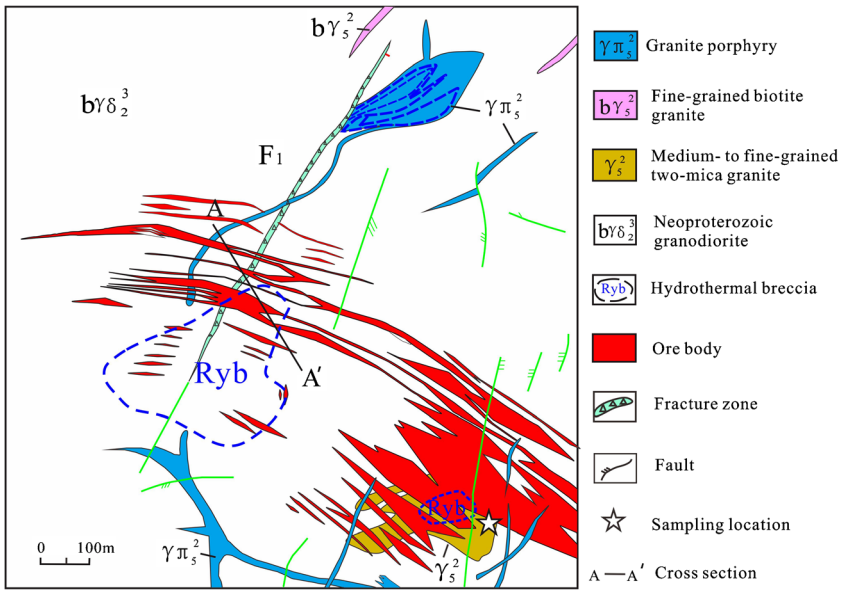

Fig. 2 Geological sketch map of the Dalingshang deposit, showing various Mesozoic granite variants and the Neoproterozoic granodiorite, as well as associated ore bodies (modified after Jiang et al. 2015)

generally correlates positively with the intensity of greisenization. Other subordinate alteration types include K-feldspar alteration in endocontact zones, and protolithionite and chlorite alteration in exocontact zones.

Besides the normal vein systems, a hydrothermal breccia pipe occurs on the top of Mesozoic granite as a result of fluid overpressure. It has a vertical lenticular shape and is composed of altered rock fragments and cementing minerals which consist almost entirely of quartz with minor chalcopyrite, molybdenite, and sphalerite (Fig. 5l; ESM Fig. 1f). The fragments (0.3–0.5 m) can be brecciated magmatic rocks of the Neoproterozoic granodiorite or Mesozoic granite. Chalcopyrite and molybdenite sometimes occur as masses, veinlets, or disseminations in cracks of quartz cements. Hydrothermal alteration in or on the edge of breccia or surrounding rocks mainly includes biotitization, greisenization, and K-feldspar alteration.

Samples and analytical methods

All samples were collected from underground tunnel #81 in the Dalingshang deposit. Sections for quartz vein, hydrothermal breccia, and ore-related granite were prepared and observed under the microscope. Representative samples were chosen for picking mineral separates for oxygen, hydrogen, or lead isotope analysis. Quartz, feldspar, muscovite, and some sulfide minerals (chalcopyrite, bornite, and molybdenite) were handpicked under a binocular microscope.

Fluid inclusion measurements

Representative samples of wolframite, scheelite, apatite, and quartz were chosen for fluid inclusion study. Fluid inclusions in wolframite were observed using an Olympus BX51 infrared microscope equipped with a high-resolution IR camera, at Wuhan Institute of Geology and Mineral Resources, China Geological Survey. The infrared microthermometric study was done on a Linkam MD600 heating/freezing stage. The accuracy is about ± 0.2 °C in cooling cycles and ± 2 °C in heating cycles. A cycling method for measurement as described by Goldstein and Reynolds (1994) was adopted.

The microthermometric measurements for scheelite, apatite, and quartz were performed using a Linkam THMSG600 heating/freezing stage mounted on a Leica DM 2500P microscope in the fluid inclusion laboratory at China University of Geosciences, Wuhan (CUGW). Temperatures were observed at 20 °C/min during freezing and heating, and less than 1 °C/min when close to phase transitions. The precision of the measurements is ± 0.2 °C from − 196 to 0 °C and ± 1 °C from 100 to 600 °C. The composition of single inclusions was identified with a Renishaw RM-1000 Raman microspectrometer at the State Key Laboratory of Geological Processes and Mineral Resources, China University of Geosciences, Wuhan (GPMR-CUGW). An Ar^+ (532.5 nm) laser with a source power of 20 mW (2 mW power on sample surface) was used.

Hydrogen and oxygen isotope analysis

The H-O isotopic compositions were analyzed using a Finnigan MAT253 mass spectrometer in the Laboratory of Stable Isotope Geochemistry, Institute of Mineral Resources, Chinese Academy of Geological Sciences in Beijing. Water in fluid inclusions was extracted from quartz separates by the decrepitation method, and then was reacted with heated chromium to release hydrogen for analysis. Oxygen isotope analyses for quartz, feldspar, muscovite, and bulk rock were performed by the conventional BrF_5 method described by

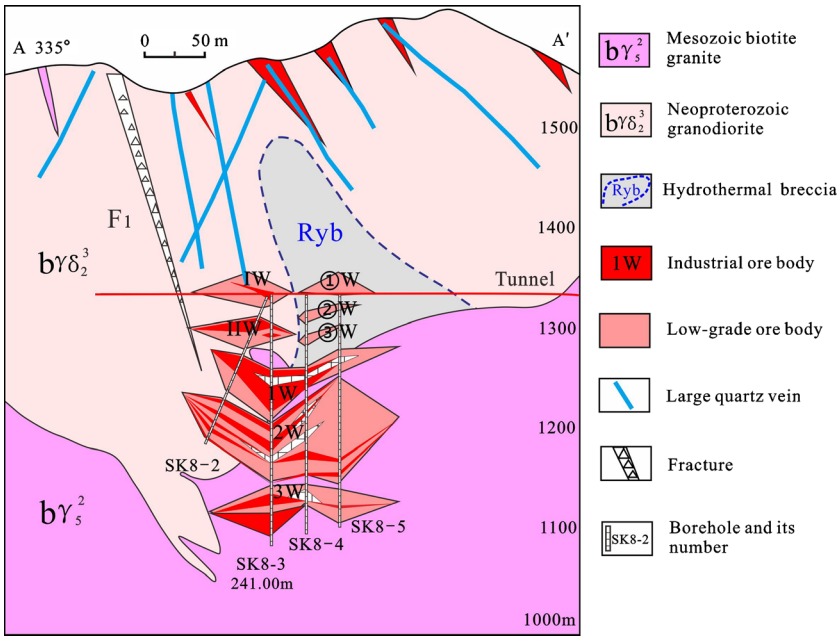

Fig. 3 Geological section of line 8 in the Dalingshang deposit, showing distribution of the major ore types

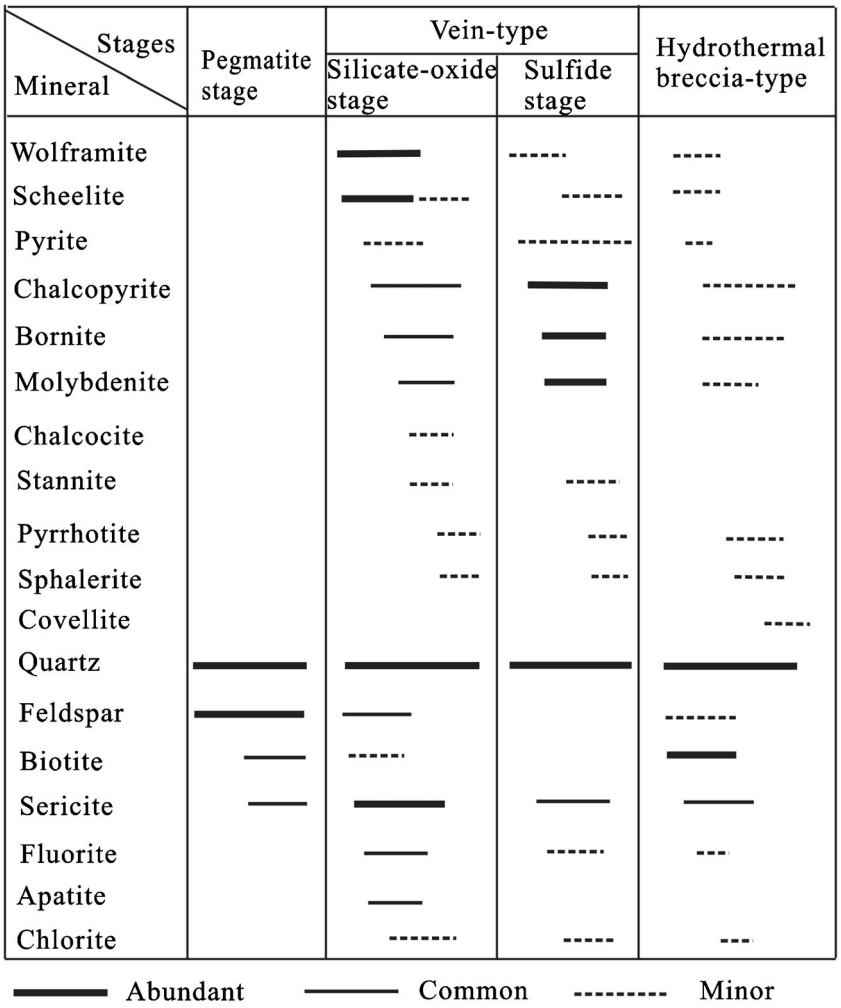

Fig. 4 Paragenetic sequence of the main minerals from the Dalingshang deposit

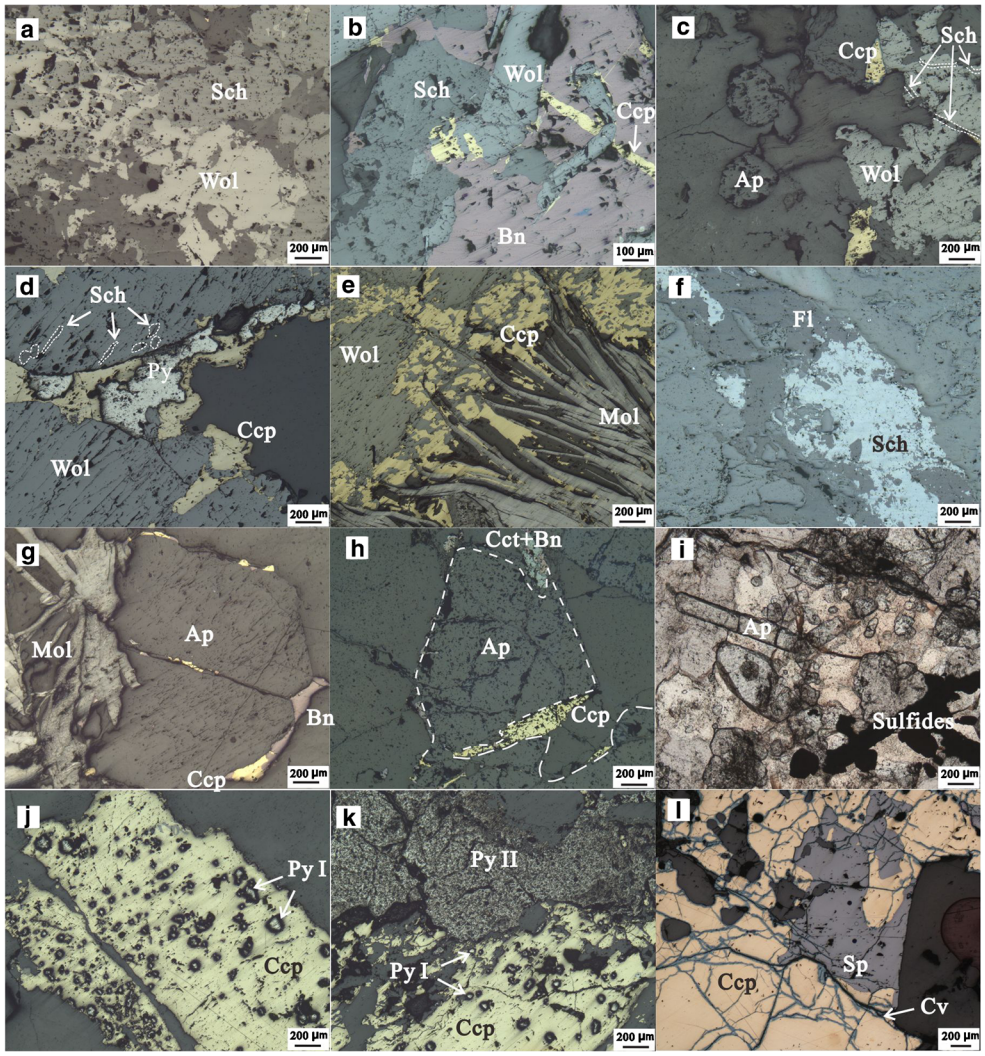

Fig. 5 Photomicrographs showing the typical composition and texture of ores in the Dalingshang deposit: silicate-oxide stage (**a**–**i**), sulfide stage (**j**–**k**), and hydrothermal breccia (**l**). **a** Intergrowth of wolframite and scheelite in mineralized quartz vein. **b** Early-precipitated wolframite and scheelite are replaced by bornite and chalcopyrite. **c** Coexisting wolframite and apatite, with wolframite replaced by chalcopyrite and microveins of scheelite. **d**, **e** Wolframite is replaced by pyrite, chalcopyrite, and molybdenite. **f** Coexisting scheelite and fluorite in veinlet. **g**–**i** Apatite is replaced by later-formed sulfide minerals, such as chalcopyrite, molybdenite, bornite, and chalcocite (**k** is under transmitted-light). **j**, **k** Ore minerals of the sulfide stage, showing chalcopyrite replacing pyrite I, and overprinted by pyrite II. **l** Ore minerals in hydrothermal breccia, showing that chalcopyrite was replaced by sphalerite, followed by covellite filling microfractures within chalcopyrite and sphalerite (*Wol* wolframite, *Sch* scheelite, *Ccp* chalcopyrite, *Bn* bornite, *Py* pyrite, *Mol* molybdenite, *Fl* fluorite, *Ap* apatite, *Cct* chalcocite, *Sp* sphalerite, *Cv* covellite)

Clayton and Mayeda (1963). All values adopted the V-SMOW standards with the error of ± 2‰ for δD and ± 0.2‰ for $\delta^{18}O$.

Sulfur isotope analysis

In-situ LA-MC-ICP-MS sulfur isotope analysis was conducted on sulfide minerals from a total of eight polished thin-sections covering different stages. Laser sampling was performed by a Resonetics-S155 excimer ArF laser ablation system, and sulfur isotope ratios were analyzed with a Nu Plasma II MC-ICP-MS at GPMR-CUGW. All analyses were made using a 30 μm laser beam with a repetition rate of 10 Hz and an ablation time of 40 s. The national pyrite standard WS-1 and the international sphalerite standard NBS-123 were used in this study. The standard-sample-standard bracketing technology was used to measure the $\delta^{34}S$ values. The true sulfur isotope ratio is calculated by correction for instrumental mass bias by linear interpolation between the biases calculated from two neighboring standard analyses. Isotope ratio data are reported relative to Vienna Cañon Diablo troilite (V-CDT) in terms of conventional per mil deviation (‰). The analytical uncertainties in this study are about 0.1‰. Detailed analytical conditions and procedures can be seen in Zhu et al. (2017).

Lead isotope analysis

The lead isotope analysis for 15 sulfide samples (chalcopyrite, molybdenite, and bornite) and 5 granitic feldspar samples were performed on a Neptune Plus MC-ICP-MS at the State Key Laboratory for Mineral Deposits Research of Nanjing University. Sulfide samples were dissolved by concentrated $HCl + HNO_3$ and feldspar samples were dissolved in concentrated $HF + HNO_3$. A two-column AG 1-X8 anion resin method was then used to separate and purify the Pb. Lead isotope ratios were measured using the Neptune Plus MC-ICP-MS and the obtained ratios were compared to the Pb reference standard NBS-981, with analytical reproducibility of 0.1‰ for $^{206}Pb/^{204}Pb$ and $^{207}Pb/^{204}Pb$, and 0.2‰ for $^{208}Pb/^{204}Pb$.

OM-CL imaging of scheelite

A total of eight polished thin-sections for in-situ LA-ICP-MS analysis were prepared from different scheelite ores of the Dalingshang deposit. The scheelite samples can be subdivided into four groups according to their field occurrence and microscopic crystal morphology. Type 1 scheelite formed in the greisenization zone of altered Mesozoic granite and can exhibit euhedral or anhedral crystal shape. Type 2 and type 3 scheelite is from the silicate-oxide stage and is hosted in veinlets from the endocontact and exocontact zones of altered granitic rocks, respectively. Type 4 scheelite is from the sulfide stage and occurs as thin veinlets crosscutting chalcopyrite. The thin sections were initially examined using a CL8200 MK5-type cathodoluminescence microscope (OM-CL) at CUGW. Extensive CL imaging reveals that almost all scheelite samples have inhomogenous CL colors within single grains, commonly with a bright CL core and large bluish CL rims (ESM Fig. 2g–i), which reflect the inhomogeneous distribution of minor elements such as REE (Brugger et al. 2000).

LA-ICP-MS analysis of trace elements in scheelite

On the basis of CL images, a total of 65 LA-ICP-MS trace element analyses were performed on 13 scheelite grains at Nanjing Focu MS Technology Co. Ltd., China. Ablation was done using a Photon Machines Excite 193 nm ArF excimer laser coupled to an Agilent 7700× ICP-MS. The ablation spot size was 40 μm in diameter, and the laser system was operated at an energy density of 6.71 J/cm^2 with a repetition rate of 7 Hz. Each analysis involves ~15 s background followed by ~40 s sample acquisition. NIST SRM 610 and 612 were used as external calibration standards for mass discrimination and time-drift sensitivity correction of the ICP-MS (Liu et al. 2008), and ^{42}Ca was used as an internal standard. Data reduction was done through *ICPMSDataCal.*

Results

Petrography and microthermometry of fluid inclusions

Representative samples of wolframite, scheelite, apatite, and quartz were chosen for fluid inclusion study. Detailed fluid inclusion petrography revealed three types of fluid inclusions: (1) liquid-rich two-phase aqueous fluid inclusions (type Ia), (2) vapor-rich two-phase aqueous fluid inclusions (type Ib), and (3) three-phase aqueous inclusions containing a solid crystal (type II). Type Ia inclusions are always the most abundant in all minerals, accounting for more than 95% of the total inclusion numbers. Type II inclusions are subordinate and represent about 4% of the total numbers. Type Ib inclusions are scarce, and only occur in a few cases in the whole sections. For ore-associated granite, some melt inclusions and fluid-melt inclusions were identified.

Microthermometric measurements of fluid inclusions in wolframite and apatite were conducted on fluid inclusion assemblages (FIA) if the inclusions were trapped along growth bands (Goldstein and Reynolds 1994; Goldstein 2003). At the Dalingshang deposit, no growth bands were observed in scheelite and quartz, and thus fluid inclusion data were obtained from primary inclusion groups which have similar heating and freezing behavior. All the type II inclusions are partially homogenized with the disappearance of vapor, and no dissolution of either opaque or transparent crystals could be observed prior to decrepitation. Coexisting type Ia, Ib, and II inclusions homogenize at roughly similar temperatures and salinities, indicating that they have been trapped at the same time and thus represent an FIA.

The salinities of fluid inclusions were estimated from ice-melting temperatures ($T_{m\text{-}ice}$) using the formula of Hall et al. (1988) for the $NaCl\text{-}H_2O$ system. The summary of microthermometric data is given in Table 1 and graphically illustrated in Fig. 6.

Fluid inclusions in the silicate-oxide stage

For the silicate-oxide stage, fluid inclusions have been studied in wolframite, scheelite, apatite, and their coexisting quartz. Only type Ia inclusions can be observed in wolframite. These inclusions generally show rounded-rectangular shape, with the vapor bubble occupying less than 30% of the total volume. They generally occur as singles or clusters within the growth bands in wolframite (ESM Fig. 3a–c), suggesting a primary origin. Infrared microthermometric study shows that fluid inclusion assemblages in wolframite have ice-melting temperatures ($T_{m\text{-}ice}$) from −4.1 to −6.3 °C, equivalent to salinities from 6.6 to 9.6 wt% $NaCl_{eq}$, and homogenization temperatures (T_h) from 310 to 369 °C.

Table 1 Summary of microthermometric data in the Dalingshang deposit, northern Jiangxi Province

Samples	Minerals	$T_{m\text{-}ice}$ (°C)[a]	Salinity (wt% $NaCl_{eq}$)	T_h (°C)[b]
Silicate-oxide stage (large vein)				
BYJ-7	Wolframite	− 5.4 to − 5.7 (10)	8.4–8.8 (10)	327–369 (11)
BYJ-10	Wolframite	− 5.8 to − 6.3 (8)	9.0–9.6 (8)	333–354 (11)
BYJ-14	Wolframite	− 4.1 to − 5.3 (17)	6.6–8.3 (17)	310–367 (25)
BYJ-9	Scheelite	− 5.3 to − 6.3 (12)	8.3–9.6 (12)	306–367 (21)
BYJ-14	Scheelite	− 4.3 to − 5.6 (8)	6.9–8.7 (8)	318–345 (8)
BYJ-9	Apatite	− 4.2 to − 5.3 (18)	6.7–8.3 (18)	276–345 (26)
BYJ-10	Apatite	− 3.7 to − 6.0 (19)	6.0–9.2 (19)	279–320 (28)
BYJ-7	Quartz	− 2.3 to − 5.3 (49)	3.9–8.3 (49)	210–343 (58)
BYJ-8	Quartz	− 2.8 to − 6.0 (41)	4.6–9.2 (41)	233–334 (48)
Silicate-oxide stage (veinlet)				
BYJ-18	Scheelite	− 0.9 to − 1.7 (18)	1.6–2.9 (18)	292–326 (20)
BYJ-19	Scheelite	− 2.1 to − 4.5 (14)	3.7–7.2 (14)	280–336 (20)
BYJ-18	Apatite	− 1.6 to − 2.7 (10)	2.7–4.5 (10)	265–298 (14)
BYJ-20	Apatite	− 2.8 to − 3.8 (14)	4.7–6.2 (14)	272–307 (21)
BYJ-18	Quartz	− 1.2 to − 3.1 (20)	2.1–5.1 (20)	205–307 (22)
BYJ-20	Quartz	− 3.0 to − 5.0 (19)	5.0 to 7.9 (19)	201–289 (24)
Sulfide stage				
BYJ-6	Quartz	− 1.6 to − 2.5 (24)	2.7–4.2 (24)	186–223 (24)
BYJ-16	Quartz	− 1.6 to − 3.7 (49)	2.7–6.0 (49)	211–309 (49)
Hydrothermal breccia				
BYJ-1	Quartz	− 2.4 to − 6.3 (31)	4.0–9.6 (31)	205–364 (36)
BYJ-2	Quartz	− 2.0 to − 5.7 (22)	3.4–8.8 (22)	197–342 (28)
BYJ-4	Quartz	− 1.5 to − 5.4 (32)	2.6–8.4 (32)	176–328 (32)

Numbers in brackets represent the number of measurements

[a] Final melting temperature of ice

[b] Total homogenization temperature of type Ia and Ib inclusions, or partial homogenization temperature of type II inclusions with a solid

Fluid inclusions in scheelite and apatite are primarily type Ia inclusions, accompanied by a few type II inclusions with an unidentified opaque solid (ESM Fig. 3d, g), and several type Ib inclusions. However, quartz coexisting with wolframite, scheelite, and apatite contains much more solid species such as chalcopyrite, muscovite, sphalerite, as well as various unidentified transparent phases. Type Ib inclusions in all minerals are scarce, characterized by subrounded shapes and high vapor volumetric proportions with a small amount of liquid attached to the dark bubble. Generally, fluid inclusion assemblages in these minerals show a variety of morphologies from rounded-rectangular, ellipsoidal shapes to rhomb or negative forms. They are always in clusters or trails, with variable size from 3 to 30 μm.

Conventional microscopic measurements of fluid inclusion assemblages in scheelite, apatite, and intergrowth quartz show that they have different salinities and temperatures (Table 1). Fluid inclusions in large quartz vein minerals have salinities varying from 6.9 to 9.6 wt% $NaCl_{eq}$ (scheelite), 6.0 to 9.2 wt% $NaCl_{eq}$ (apatite), and 3.9 to 9.2 wt% $NaCl_{eq}$ (quartz), respectively. Their T_h values show values from 306 to 367, 276 to 345, and 210 to 343 °C, respectively. The calculated salinities of fluid inclusions in veinlet minerals are mainly in the range of 1.6–7.2 wt% $NaCl_{eq}$ (scheelite), 2.7–6.2 wt% $NaCl_{eq}$ (apatite), and 2.1–7.9 wt% $NaCl_{eq}$ (quartz), respectively. Their measured T_h values are in the range of 280–336, 265–307, and 201–307 °C, respectively.

Fluid inclusions in the sulfide stage

For the sulfide stage, only fluid inclusions in quartz can be observed and analyzed. Type Ia inclusions and a few type II inclusions with chalcopyrite are observed. Fluid inclusion assemblages in this stage yield distinctly lower salinities and temperatures than those of quartz in the silicate-oxide stage (Table 1). The estimated salinities using the $T_{m\text{-}ice}$ values range from 2.7 to 6.0 wt% $NaCl_{eq}$, whereas the measured T_h values are in the range of 186–309 °C.

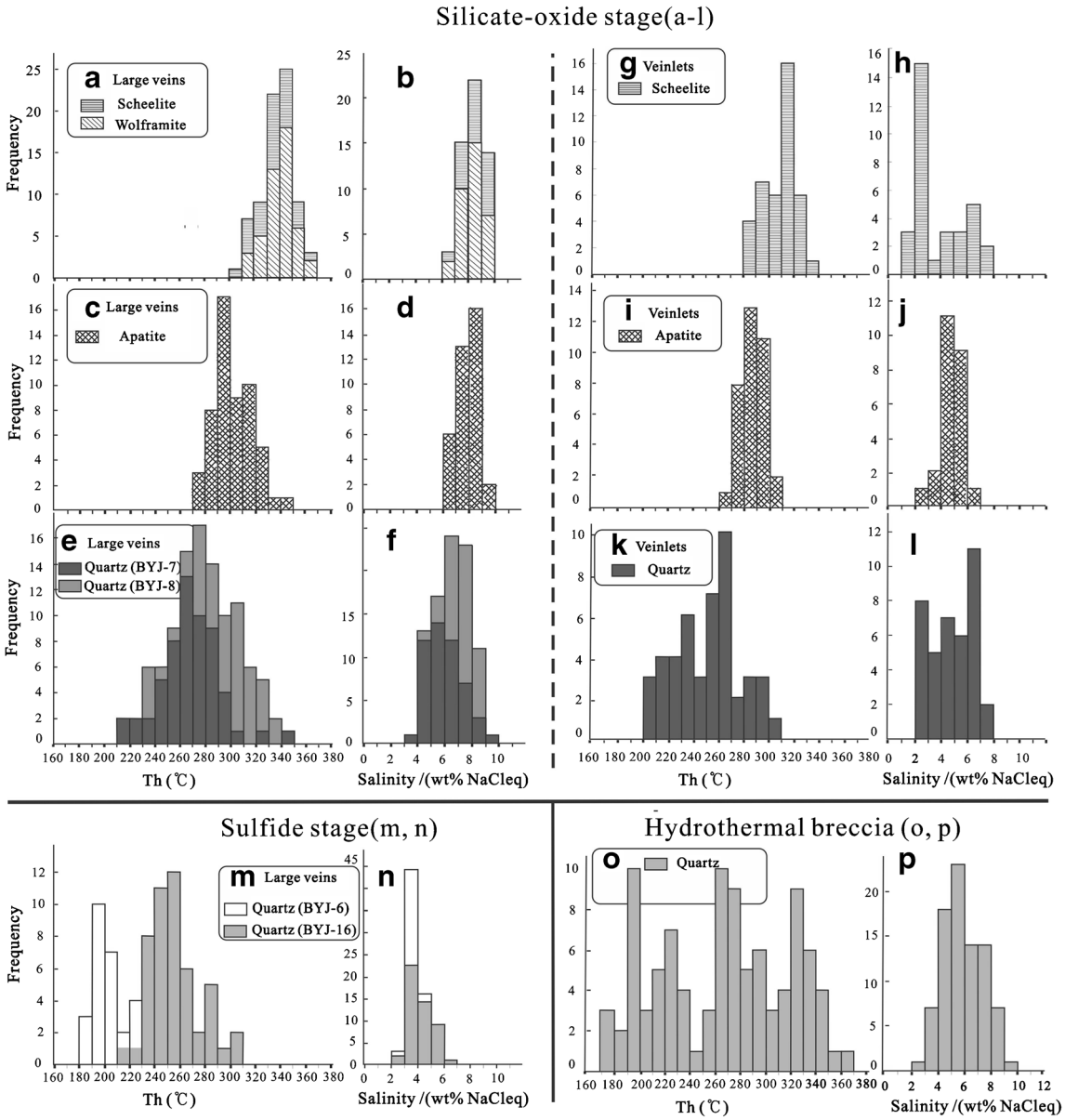

Fig. 6 Histograms of homogenization temperatures (left) and salinities (right) of fluid inclusion assemblages from different ore stages in the Dalingshang deposit

Fluid inclusions in hydrothermal breccia

Fluid inclusions in hydrothermal breccia have comparatively larger sizes (5–40 μm) with more irregular shapes compared to fluid inclusions in quartz veins (ESM Fig. 3l). Type Ia inclusions account for more than 98% of the total inclusion numbers, whereas type Ib and II inclusions only occur in a few cases. The solid species in type II inclusions can be crystals of chalcopyrite or muscovite.

In the hydrothermal breccia, fluid inclusion assemblages have salinity values ranging from 2.6 to 9.6 wt% $NaCl_{eq}$. They are totally homogenized at temperatures of 176–364 °C with a tri-modal distribution of T_h values, including the low T_h region from 170 to 240 °C, the middle T_h region from 250 to 300 °C, and the high T_h region from 310 to 360 °C.

Fluid/melt inclusions in Mesozoic two-mica granite

Fluid inclusions recognized in phenocrysts and matrix quartz from ore-related Mesozoic granite have almost the same features and microthermometric results as those from veinlets, indicating that the granites are affected by hydrothermal fluid overprint. Noticeably, some melt inclusions and fluid-melt inclusions have been recognized. Melt inclusions in the Dalingshang granite consist of melt ± daughter minerals ± one or more vapor bubbles (ESM Fig. 4a–e). They show subrounded or negative-crystal morphologies, varying in size

from 10 to 100 μm. The melt inclusions can be subdivided into glassy and crystallized. Glassy melt inclusions show relatively bright color and sharp borders under the microscope (ESM Fig. 4a–c). They have a round or elliptical vapor bubble distributed in the middle or at the edge of the silicate glass. Some of the glass has undergone devitrification to form microlites, characterized by distinctly brown color (or faint spots) under crossed polars (ESM Fig. 4b). Crystallized melt inclusions (10–40 μm) account for the majority of the total melt inclusions. They generally have rough boundaries and always show an overall sparkly appearance under crossed polars, with the elliptical bubble at the edge of the crystalline component (e.g., albite, muscovite, quartz, and monazite) (ESM Fig. 4d–e). Occasionally, several distorted bubbles may occur in one single melt inclusion. Fluid-melt inclusions comprise melt ± daughter minerals ± aqueous fluid with a shrinkage bubble (ESM Fig. 4f–i). They commonly show irregular or subcircular shape with a size range of 10–30 μm. The aqueous fluid has variable proportions (10–50%) and is generally distributed around the edge of the melt.

Laser Raman microprobe results

Melt inclusions in phenocrysts and interstitial quartz from the ore-related granite have $CH_4 + N_2$ as gas phase as indicated by Raman spectra (ESM Fig. 5a). Fluid inclusions in scheelite and quartz of the silicate-oxide stage contain CH_4 and N_2 only, without CO_2 (ESM Fig. 5b–d), while fluid inclusions from the sulfide stage contain variable CO_2 contents with estimated CH_4/CO_2 ratios varying from 0.97 to 2.83 (ESM Fig. 5e). In the hydrothermal breccia, vapor compositions are composed primarily of $CH_4 + N_2$ with trace CO_2 (ESM Fig. 5f). Thus, it seems that CH_4 was the exclusive carbon species in the early magmatic and hydrothermal fluids, but there is a clear CO_2 component in the late stage of mineralization as fluids evolved.

Solid phases detected within melt inclusions and fluid-melt inclusions in phenocrysts and interstitial quartz comprise crystals of albite, muscovite, quartz, monazite, chalcopyrite, and rutile (ESM Fig. 5g–j). In samples from different styles of ores, chalcopyrite, muscovite, and sphalerite are the most abundant daughter minerals recognized in fluid inclusions (ESM Fig. 5j–l).

Hydrogen-oxygen isotope data

The analytical results on H-O isotopes of hydrothermal quartz from orebodies and the igneous minerals from the ore-related granites are listed in ESM Table 2. The ore fluids have measured δD values from − 81 to − 102‰. The oxygen isotope data of fluids in equilibrium with the quartz were calculated using the quartz-water equation of Clayton et al. (1972). The calculations yield $\delta^{18}O_{water}$ values ranging from 0.2 to 5.1‰ and the data are plotted in Fig. 7. The oxygen isotope compositions of igneous quartz, plagioclase, and muscovite minerals from the fresh two-mica granites yield $\delta^{18}O$ values of 12.5–13.2, 10.1–11.3, and 10.7–11.1‰, respectively. Three whole rock $\delta^{18}O$ values fall in the range of 10.8–11.5‰.

Sulfur isotope composition of the sulfides

This paper is the first to carry out in-situ LA-MC-ICP-MS sulfur isotope analysis on sulfides in the Dahutang district. The sulfur isotopic compositions are shown in ESM Table 3 and Fig. 8. The $\delta^{34}S$ values range from − 4.1 to 1.3‰ for sulfides of the silicate-oxide stage, and − 3.1 to − 1.2‰ for hydrothermal breccia. However, for the sulfide stage, sulfides exhibit a large variation in $\delta^{34}S$ values of pyrite I from − 2.1 to − 0.9‰, chalcopyrite from − 5.8 to − 1.6‰, and pyrite II from − 14.4 to − 7.5‰ (ESM Table 3).

Lead isotope composition of the sulfides and granite

The Pb isotope data for selected sulfides and granitic feldspars are listed in ESM Table 4 and plotted in Fig. 9. The measured $^{206}Pb/^{204}Pb$, $^{207}Pb/^{204}Pb$, and $^{208}Pb/^{204}Pb$ ratios for the sulfides vary from 18.067 to 18.566, 15.611 to 15.757, and 38.334 to 38.862, respectively. Feldspars from the Dalingshang granites are characterized by much broader variation of $^{206}Pb/^{204}Pb$, $^{207}Pb/^{204}Pb$, and $^{208}Pb/^{204}Pb$ ratios, with a range from 18.210 to 19.127, 15.617 to 15.791, and 38.555 to 39.660, respectively.

Trace element concentrations in scheelite

The trace element data of scheelite are given in ESM Table 5 and the chondrite-normalized REE patterns for representative scheelite samples are shown in ESM Fig. 6. The scheelite from Dalingshang has low concentrations of Mo (< 0.01–28 ppm), Sn (< 0.01–17 ppm), Cu (< 0.01–28 ppm), Zn (<

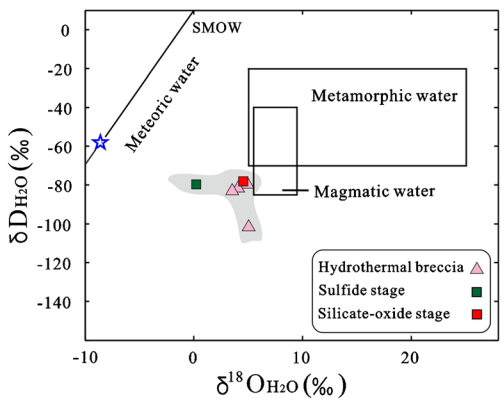

Fig. 7 δD_{H2O}-$\delta^{18}O_{H2O}$ plot of ore-forming fluids in the Dalingshang deposit

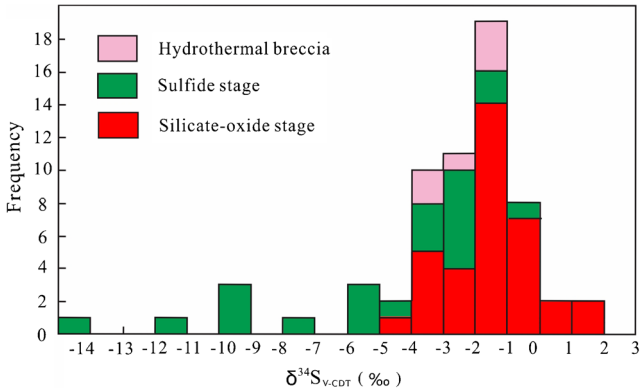

Fig. 8 Histogram of sulfur isotope compositions of sulfide minerals from the Dalingshang deposit

0.01–4 ppm), Na (< 0.01–194 ppm), Pb (0.5–20 ppm), and Rb (< 0.01–34 ppm), but high concentrations of Sr (111–2984 ppm). From scheelite type 1 to type 4, there is a decreasing trend of REE abundance from 1056 to 0.20 ppm, Y from 484 to 0.16 ppm, LREE/HREE from 4.30 to 0.51, and $(La/Lu)_N$ from 4.05 to 0.15, but an increasing trend of Nb/Ta ratio from 12 to 102, and Y/Ho ratio from 12 to 393.

The calculated Eu/Eu^*_N values of scheelite range from 0.54 to 34, and each scheelite type has both negative and positive Eu anomalies. The most striking phenomenon is that most samples are characterized by two distinct REE_N patterns within single scheelite grains: the center zone with bright CL exhibits hump-shaped (MREE-enriched) or flat (relatively MREE depleted) patterns with negative or small positive Eu anomaly, whereas the vast blue CL rims display flat REE_N patterns with variable positive Eu anomaly (ESM Fig. 6). The Dalingshang scheelite samples change their shape of the REE patterns from convex upward to downward, which is also revealed by the negative correlation of the LREE and HREE slopes illustrated in the $(Ho/Lu)_N$ vs. $(La/Sm)_N$ diagram (ESM Fig. 7b).

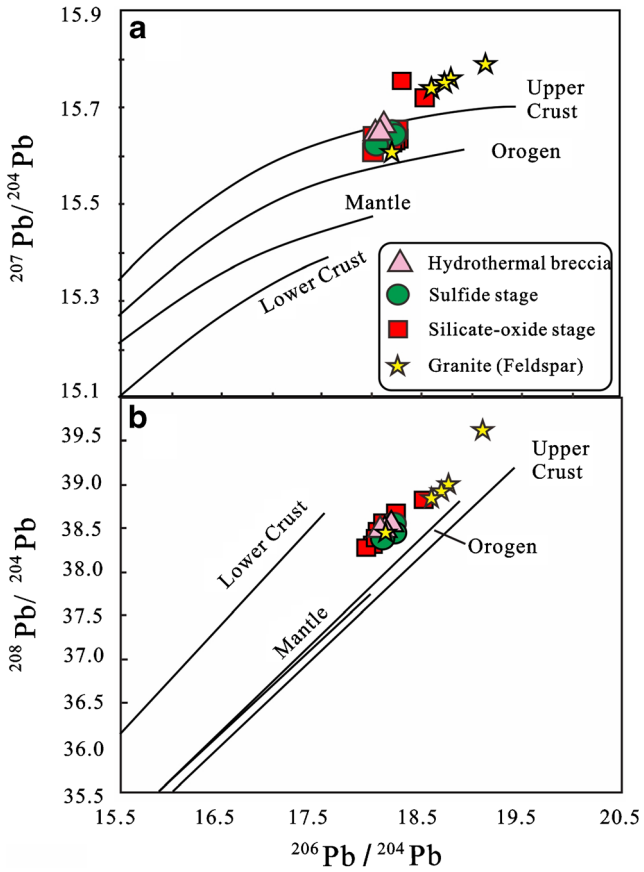

Fig. 9 Plots of lead isotope compositions in the Dalingshang deposit (after Zartman and Doe 1981)

Discussion

Sources of sulfur and lead

The sulfides from the silicate-oxide stage show quite uniform $\delta^{34}S$ values (ESM Table 3, Fig. 8), which is consistent with previously published data of the adjacent Shimensi deposit ($\delta^{34}S = -3.1$ to 1.0‰; Xiang et al. 2013). A narrow range of $\delta^{34}S$ values with a mean close to 0 is indicative of a possible magmatic source for sulfur. However, sulfides from the sulfide stage show a wide spread of $\delta^{34}S$ values with pyrite I from −2.1 to −0.9‰, chalcopyrite from −5.8 to −1.6‰, and pyrite II from −14.4 to −7.5‰ (ESM Table 3). The $\delta^{34}S$ data tend to shift toward more negative values with progressive precipitation of sulfide minerals. This large variation of sulfur isotopic composition within and between mineral grains indicates that biogenic sulfur was not likely involved during sulfide precipitation. Instead, this variation may be attributed to changes in fO_2 and pH as the fluids evolved (Rye and Ohmoto 1974; Rajabpour et al. 2017). Based on the models of Ohmoto (1972), we propose that the depleted sulfur isotope values are likely generated by an increase of oxygen fugacity due to inflow of oxidized meteoric waters, which is also indicated by the occurrence of CO_2 (transition $CH_4 \rightarrow CO_2$) in fluid inclusions from the sulfide stage (ESM Fig. 5e).

The Pb isotope data for sulfides and feldspars from the Dalingshang deposit plot are similar (Fig. 9), suggesting a similar origin and evolution history between ores and granites. Moreover, Jiang et al. (2015) reported Sm-Nd isotope analyses of scheelite in the adjacent Shiweidong deposit, yielding $^{143}Nd/^{144}Nd$ isotope values that vary from 0.512152 to 0.512289, with the inferred initial Nd isotopic compositions ($\varepsilon Nd_{142.4Ma} = -8.9$ to −8.7) in close agreement with the whole-rock data of corresponding granites (Huang and Jiang 2014). All these data tend to confirm a magmatic source for both sulfides and tungsten for the deposits in the Dahutang district.

Sources of ore-forming fluids

In the δD_{H2O}-$\delta^{18}O_{H2O}$ diagram (Fig. 7), the data fall close to the magmatic field with the $\delta^{18}O$ values in the sulfide stage largely deviating to the meteoric water line, suggesting that the early fluids are likely of magmatic origin, with possible later mixing of meteoric water. A consistent feature of fluid inclusion studies in the district are some anomalously low δD fluids (Gong et al. 2015; Ye et al. 2017). This phenomenon can be explained by (1) low δD meteoric water that originated at high altitudes, (2) magma degassing and resultant deuterium-depleted magmatic waters (Nabelek et al. 1983), (3) boiling/vapor separation of ore fluids, and (4) fluid interaction with reducing sediments that are rich in organic material or NH^{4+}-rich micas (e.g., Polya et al. 2000; Dewaele et al. 2016). Considering the low paleolatitude of the Dahutang district, the common existence of CH_4 and N_2 in fluid inclusions, and that there is no evidence for boiling, the last possibility is favored here. Namely, the low δD fluids may have underwent extensive exchange with, or at least partially equilibrated, with the pelitic metasediments in the district.

In our study, the discovery of melt/fluid inclusions in phenocryst and interstitial quartz from ore-related granite is of great significance. Coexisting melt inclusions and primary fluid inclusions may imply the coexistence of silicate melt and aqueous fluids during mineral precipitation (Roedder 1979, 1992), while fluid-melt inclusions, especially those with large liquid proportions (ESM Fig. 4f–i), provide direct evidence for heterogeneous trapping of such two endmembers (Frezzotti 1992, 2001; Kamenetsky 2006). Taken together, it can be inferred that the melt and fluid-melt inclusions in two-mica granite at Dalingshang were trapped at the magmatic-hydrothermal transition (Halter and Webster 2004; Veksler 2004).

Noticeably, melt-volatile fluid immiscibility has long been considered as an important process in many magmatic-hydrothermal systems, since the volatile phases exsolved can carry significant amounts of metallic elements, which is one of the essential steps for economic enrichment of W, Sn, Cu, Mo, and other metals in hydrothermal fluids (Shinohara 1994; Bodnar 1995; Harris et al. 2003; Kamenetsky et al. 2003, 2004; Student and Bodnar 2004; Webster 2004; Webster and Thomas 2006). At Dalingshang, chalcopyrite is commonly observed as solid in melt inclusions from granite and later-formed fluid inclusions from different types of ores. This may indicate that the hydrothermal fluids had inherited considerable amounts of ore metals when they exsolved from the residual melts. Thus, we conclude that the ore-bearing fluids at Dalingshang were likely originally derived from exsolving fluids during the magmatic-hydrothermal transition, locally in equilibration with residual organic-rich metasediments, and probably diluted by meteoric water in the late sulfide stage as supported by H-O isotopes.

Comparison of fluid inclusions in ore and gangue minerals

The fluid inclusion data indicate that ore and gangue minerals at Dalingshang formed at different temperatures. During the silicate-oxide stage (Fig. 6a–l), the homogenization temperature of fluid inclusions in wolframite (310 to 370 °C, peak at 330 to 350 °C) is similar to scheelite, but about 40 °C higher than that of coexisting apatite (270 to 340 °C, peak at 290 to 310 °C) and generally 70 °C higher than that in adjacent quartz (210 to 340 °C, peak at 260 to 280 °C). For the sulfide stage, fluid inclusions in quartz yield lower temperatures (180 to 310 °C) and salinities than those hosted in quartz of the silicate-oxide stage (Fig. 6m, n).

These results indicate that wolframite and scheelite were likely deposited earlier than the coexisting quartz, which is also supported by the textural evidence that wolframite and scheelite commonly occur in the margins of veins whereas quartz is in the center (ESM Fig. 1b–d). No high-salinity inclusions were recorded in any minerals, and the fluids trapped are characterized by high- to medium-temperature, low-salinity, CH_4, N_2, and/or CO_2-bearing aqueous fluids, with a trend from CH_4 to CO_2 with time and decreasing temperature.

Fluid inclusions can provide key information about roles of fluids during ore-forming processes. Combined with the δD_{H2O}-$\delta^{18}O_{H2O}$ data (Fig. 7), the temperature vs. salinity plot (Fig. 10), and the mixing models of oxygen isotope effects using the methods of Wagner et al. (2009) (Fig. 11), we suggest that different fluid processes were involved in the progressive precipitation of metals: scheelite (and wolframite) hosted in both large veins and small veinlets formed by simple cooling; in contrast, increasing involvement of meteoric waters may have taken place in later-formed quartz and fluid mixing is likely an effective mechanism triggering successive deposition of base metal sulfides. However, the hydrothermal breccia may have undergone a somewhat more complicated evolution history (Fig. 10d). The three discrete fluid inclusion populations and the multi-modal distribution of temperatures probably indicate its formation by multiple pulses of vein opening and brecciation. Nevertheless, boiling can be excluded as an effective way for metal deposition since no fluid inclusion evidence was available for effervescence in spite of the structural setting for transition from a relatively closed to an open system.

Fluid-rock interaction deduced from scheelite trace element evidence

Generally, the Eu anomaly in scheelite can be either inherited from the primary fluid, or modified by chemical variations of a single fluid during scheelite precipitation and fluid-rock interaction (Ghaderi et al. 1999; Brugger et al. 2000, 2008). Most scheelite samples at Dalingshang have inhomogeneous

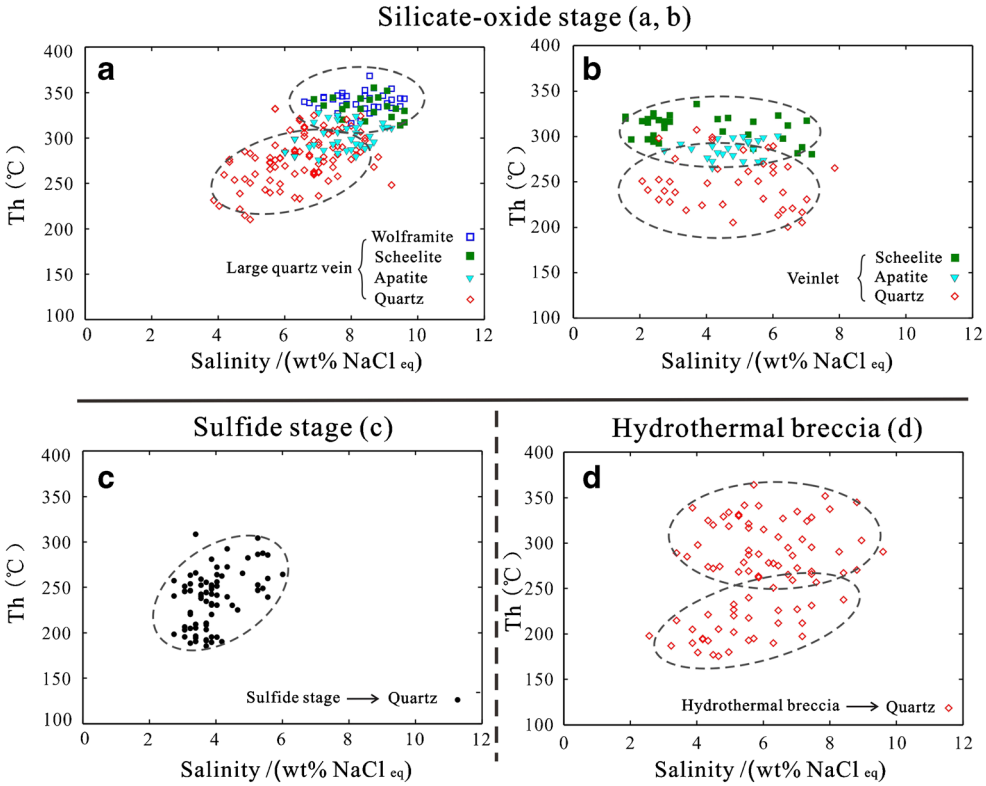

Fig. 10 Homogenization temperature versus salinity of fluid inclusion assemblages from different ore stages

distribution of Eu anomalies with relatively negative Eu/Eu* values for the grain cores and positive Eu/Eu* values for the large rims (ESM Fig. 6). Given the fact that scheelite is mostly developed in veinlets associated with the altered wall rock, not in the large quartz veins, we suggest that the negative Eu anomalies were inherited from distinct pulses of "fresh" hydrothermal solutions derived from the granites, and the positive Eu anomalies are due to the release of Eu^{2+} caused by decomposition of feldspar. Fluid-rock interaction could have provided a large amount of Ca, Eu, and Sr for the W-rich fluids to form scheelite. The transition of patterns from parabolic to flat within single scheelite grains, as indicated by the $(Ho/Lu)_N$ vs. $(La/Sm)_N$ diagram (ESM Fig. 7b), may result from the preferential removal of MREE during scheelite growth, since scheelite has a preference for MREEs, and the precipitation of scheelite may progressively produce a MREE-depleted fluid (Brugger et al. 2000; Hazarika et al. 2016).

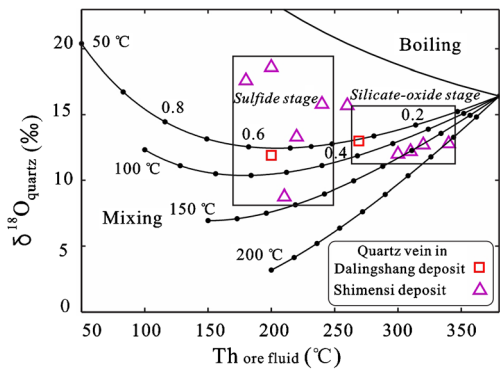

Fig. 11 Diagrams showing the effect of mixing on $\delta^{18}O$ composition of quartz in equilibrium with a magmatic-hydrothermal fluid (initial $\delta^{18}O$ = 11.9‰, T = 380 °C), which is mixed with meteoric water ($\delta^{18}O$ = −8.5‰, at 50, 100, 150, and 200 °C, respectively). Also shown are temperature and oxygen isotope data of quartz from the Shimensi deposits in the Dahutang ore field (Gong et al. 2015)

Implications for ore genesis

The northern Jiangnan Orogen is a recently discovered tungsten ore belt in northeastern South China and is the host for several large to super-large tungsten deposits, including the Yangchuling W-Mo, Xianglushan W, Dahutang W-Cu, and Zhuxi W-Cu deposits. These deposits are all associated with Late Jurassic to Early Cretaceous (150–126 Ma) granite magmatism (Jiang et al. 2015; Pan et al. 2017; Mao et al. 2017; Zhao et al. 2017), temporally coeval with the nearby Middle-Lower Yangtze River Valley porphyry and skarn Cu-Fe-Au-Mo belt (Xie et al. 2012; Cao et al. 2017). Previous studies have shown that northeastern South China was dominated by an extensional setting associated with lithospheric thinning and asthenospheric upwelling at that time (Li 2000; Li et al. 2008; Ling et al. 2009; Jiang et al. 2011; Mao et al. 2013). Accordingly, the Late Jurassic to Early Cretaceous granites associated with W mineralization in the Jiangnan tungsten ore belt were likely related to the same extensional

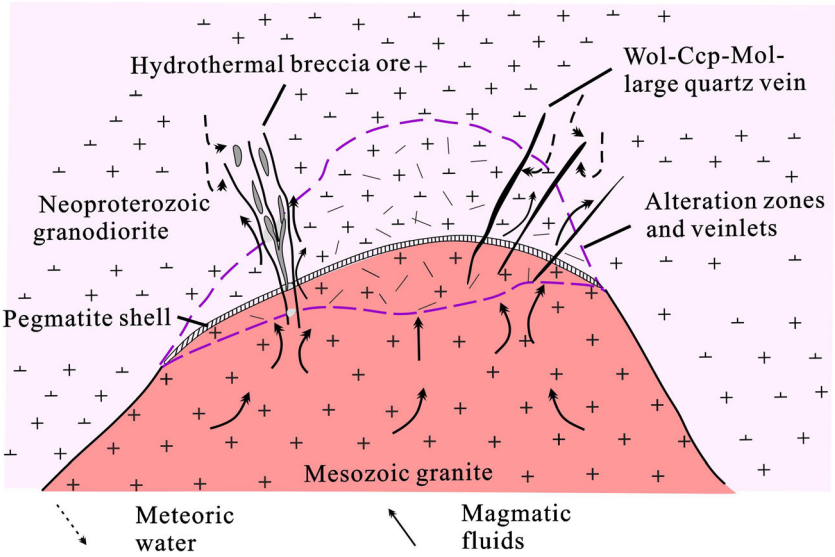

Fig. 12 An idealized model for the formation of major mineralization styles in the Dalingshang deposit

processes and have been interpreted as generated by partial melting of the continental crust (Mao et al. 2015, 2017; Zhao et al. 2017).

The ore-related granites have high whole-rock $\delta^{18}O$ values ranging from 10.8 to 11.5‰, which is consistent with the S-type affinity and partial melting of continental crust. The low Fe^{3+}/Fe^{2+} ratios for biotite (Huang and Jiang 2014), the predominance of $CH_4 + N_2$ over CO_2 in fluid inclusions, and the low Mo content in scheelite all support a relatively reduced environment (Hsu and Galli 1973) for the Dalingshang ore system. The low-oxygen fugacity condition may exert essential roles for tungsten mineralization since it can not only favor enrichment of tungsten in silicate liquids during source melting and magmatic differentiation but also promote the extracting efficiency of W from melts into ore fluids and generally contribute to mineral deposits with high W/(Cu + Mo) ratio (Candela 1992).

Globally, the tungsten mineralogy in different W deposits always shows common features depending on the nature of wall rock: wolframite-bearing veins are generally hosted in iron-bearing pelitic rocks, whereas scheelite deposits in skarns are related to calcareous rocks (Kwak 1987; Lecumberri-Sanchez et al. 2017; Soloviev and Kryazhev 2017). In contrast to skarn deposits, the highest tungsten grades at Dahutang are associated with scheelite-bearing veinlets in the Neoproterozoic granodiorite without skarn replacement. Instead, extensive hydrothermal alteration including greisenization, alkali-feldspathization, protolithionite, and chloritization are widely developed around ore bodies. The Neoproterozoic granodiorite is documented as Ca-rich (CaO = 1.63–2.05 wt%) and with plagioclase high in An (29.7–44.3, average 38.8, Wang et al. 2015), different from the Mesozoic granites. Based on field geological relationships, mineralogical features, and the evidence of scheelite trace elements, we suggest that fluid-rock interaction is one of the most important mechanisms for tungsten mineralization in this giant tungsten district, in terms of providing the large amounts of calcium required for scheelite precipitation. Finally, we note that the Dalingshang is a vein-type tungsten deposit with a hydrothermal breccia developed in the apical fracture zone, and an idealized model is proposed in Fig. 12 to explain the major mineralization styles.

Conclusions

1) Sulfur and lead isotope composition of sulfides implies a magmatic source for the W-Cu mineralization in the Dalingshang deposit. The depleted $\delta^{34}S$ values of sulfides in the sulfide stage were likely generated by an increase of oxygen fugacity of the ore fluids due to mixing with meteoric water.
2) Homogenization temperatures for primary inclusions in wolframite are similar to those in scheelite, but about 40 °C higher than those of apatite and generally 70 °C higher than those in coexisting quartz. The mineralizing fluids trapped in these minerals are overall characterized by high to medium temperature, low salinity, CH_4, N_2, and/or CO_2-bearing aqueous fluids.
3) The low-oxygen fugacity condition in the early hydrothermal system (with CH_4) may be an important mechanism for tungsten mineralization. CO_2 does only occur in the sulfide stage after the bulk of the tungsten had been deposited.
4) The Ca component of scheelite was most likely released from break-down of plagioclase during the process of greisenization and alkali-feldspar metasomatism, and fluid-rock interaction was critical for scheelite deposition.

Acknowledgements We gratefully acknowledge Prof. Bernd Lehmann and two anonymous reviews for their constructive comments that significantly improved the manuscript. We also give special thanks to managements and staffs of the Northwest Jiangxi Geological Team and the 916 Geological Team for their helpful assistance during field work. Sincere thanks are also due to Xo-Bo Zhang, Mou-Chun He, Da Yang, Yao-Ming Xu, and Sheng-Ke Yang for their guidance and advice on experimental work. This work was financially supported by the National Key R&D Program of China (No. 2017YFC0601404), the National Science Foundation of China (No. 41473042), and the MOST Special Fund from the State Key Laboratory of Geological Processes and Mineral Resources (MSFGPMR03-2).

References

BGMRJX (1984) Regional geology of Jiangxi Province. Geological Publishing House, Beijing, pp 1–921 **(in Chinese)**

Bodnar RJ (1995) Fluid-inclusion evidence for a magmatic source for metals in porphyry copper deposits. In: Thompson JFH (ed), Magmas, Fluids, and Ore Deposits. Mineral Assoc Can Short Course Ser 23, pp 139–152

Brugger J, Bettiol A, Costa S, Lahaye Y, Bateman R, Lambert D, Jamieson D (2000) Mapping REE distribution in scheelite using luminescence. Mineral Mag 64:891–903

Brugger J, Etschmann B, Pownceby M, Liu W, Grundler P, Brewe D (2008) Oxidation state of europium in scheelite: tracking fluid-rock interaction in gold deposits. Chem Geol 257:26–33

Brugger J, Lahaye Y, Costa S, Lambert D, Bateman R (2000) Inhomogeneous distribution of REE in scheelite and dynamics of Archaean hydrothermal systems (Mt Charlotte and Drysdale gold deposits, Western Australia). Contrib Mineral Petrol 139:251–264

Candela PA (1992) Controls on ore metal ratios in granite-related ore systems: an experimental and computational approach. T Roy Soc Edin-Earth 83:317–326

Cao Y, Gao FP, Du YS, Du YL, Pang ZS (2017) Genesis of the Datuanshan stratabound skarn cu(-Mo) deposit, middle-lower Yangtze Valley, eastern China: constraints from geology, Re-Os geochronology, mineralogy, and sulfur isotopes. Mineral Deposita 52:443–462

Clayton RN, Mayeda TK (1963) The use of bromine pentafluoride in the extraction of oxygen from oxides and silicates for isotopic analysis. Geochim Cosmochim Acta 27:43–52

Clayton RN, O'Neil JR, Mayeda TK (1972) Oxygen isotope exchange between quartz and water. J Geophys Res 77:3057–3067

Dewaele S, Clercq FD, Hulsbosch N, Piessens K et al (2016) Genesis of the vein-type tungsten mineralization at Nyakabingo (Rwanda) in the Karagwe-Ankole belt, Central Africa. Mineral Deposita 51:283–307

Feng CY, Zhang DQ, Xiang XK, Li DX, Qu HY, Liu JN, Xiao Y (2012) Re-Os isotopic dating of molybdenite from the Dahutang tungsten deposit in northwestern Jiangxi Province and its geological implication. Acta Petrol Sin 28:3858–3868 **(in Chinese with English abstract)**

Frezzotti ML (1992) Magmatic immiscibility and fluid phase evolution in the Mount Genis granite (southeastern Sardinia, Italy). Geochim Cosmochim Acta 56:21–23

Frezzotti ML (2001) Silicate-melt inclusions in magmatic rocks: applications to petrology. Lithos 55:273–279

Gao LZ, Huang ZZ, Ding XZ, Liu YX, Pang JE, Zhang CH (2012) Zircon SHRIMP U-Pb dating of Xiushui and Majianqiao formations in northwestern Jiangxi Province. Geol Bull China 31:1086–1093 **(in Chinese with English abstract)**

Ghaderi M, Palin JM, Campbell IH, Sylvester PJ (1999) Rare earth element systematics in scheelite from hydrothermal gold deposits in the Kalgoorlie-Norseman region, Western Australia. Econ Geol 94: 423–437

Goldstein, RH (2003) Petrographic analysis of fluid inclusions. In: Samson I, Anderson A, Marshall D (eds) Fluid inclusions: Analysis and Interpretation. Mineral Assoc Canada, Short Course 32, pp 9–53

Goldstein RH, Reynolds TJ (1994) Systematics of fluid inclusions in diagenetic minerals. Society of Sedimentary Geology, SEPM Short Course 31:1–199

Gong XD, Yan GS, Ye TZ et al (2015) A study of ore-forming fluids in the Shimensi tungsten deposit, Dahutang tungsten polymetallic ore field, Jiangxi Province, China. Acta Geol Sin-Eng 89:822–835

Hall DL, Sterner SM, Bodnar RJ (1988) Freezing point depression of NaCl-KCl-H_2O solutions. Econ Geol 83:197–202

Halter WE, Webster JD (2004) The magmatic to hydrothermal transition and its bearing on ore-forming systems. Chem Geol 210:1–6

Harris AC, Kamenetsky VS, White NC, van Achterbergh E, Ryan CG (2003) Melt inclusions in veins: linking magmas and porphyry Cu deposits. Science 302:2109–2111

Hazarika P, Mishra B, Pruseth KL (2016) Scheelite, apatite, calcite and tourmaline compositions from the late Archean Hutti orogenic gold deposit: implications for analogous two stage ore fluids. Ore Geol Rev 72:989–1003

Hsu LC, Galli PE (1973) Origin of the scheelite-powellite series of minerals. Econ Geol 68:681–696

Huang LC, Jiang SY (2012) Geochroronology, geochemistry and petrogenesis of the porphyric like two-mica granite in the Dahutang tungsten deposit, Jiangxi Province. Acta Petrol Sin 28:3887–3900 **(in Chinese with English abstract)**

Huang LC, Jiang SY (2013) Geochronology, geochemistry and petrogenesis of the tungsten-bearing porphyritic granite in the Dahutang tungsten deposit, Jiangxi Province. Acta Petrol Sin 29:4323–4335 **(in Chinese with English abstract)**

Huang LC, Jiang SY (2014) Highly fractionated S-type granites from the gaint Dahutang tungsten deposit in Jiangnan Orogen, Southeast China: geochronology, petrogenesis and their relationship with W-mineralization. Lithos 202-203:207–226

Jiang SY, Peng NJ, Huang LC, Xu YM, Zhan GL, Dan XH (2015) Geological characteristic and ore genesis of the giant tungsten deposits from the Dahutang ore-concentrated district in northern Jiangxi Province. Acta Petrol Sin 31:639–655 **(in Chinese with English abstract)**

Jiang YH, Zhao P, Zhou Q, Liao SY, Jin GD (2011) Petrogenesis and tectonic implications of early cretaceous S- and A-type granites in the northwest of the Gan-Hang rift, SE China. Lithos 121:55–73

Kamenetsky VS (2006) Melt inclusion record of magmatic immiscibility in crustal and mantle magmas. In: Webster JD (ed), Melt Inclusions in Plutonic Rocks. Miner Assoc Canada Short Course Ser 36, pp 81–98

Kamenetsky VS, De Vivo B, Naumov VB et al (2003) Magmatic inclusions in the search for natural silicate-salt melt immiscibility: methodology and examples. In: De Vivo B, Bodnar RJ (eds) Melt inclusions in volcanic systems: methods, applications and problems, developments in volcanology vol 5. Elsevier, Amsterdam, pp 65–82

Kamenetsky VS, Naumov VB, Davidson P, van Achterbergh E, Ryan CG (2004) Immiscibility between silicate magmas and aqueous fluids: a melt inclusion pursuit into the magmatic-hydrothermal transition in the Omsukchan granite (NE Russia). Chem Geol 210:73–90

Kwak TAP (1987) W-Sn skarn deposits and related metamorphic skarns and granitoids: developments in economic geology 24. Elsevier Science, Amsterdam, pp 1–468

Lecumberri-Sanchez P, Vieira R, Heinrich CA, Pinto F, W lle M (2017) Fluid-rock interaction is decisive for the formation of tungsten deposits. Geology 45:579–582

Li XH (2000) Cretaceous magmatism and lithospheric extension in Southeast China. J Asian Earth Sci 18:293–305

Li JW, Zhao XF, Zhou MF, Vasconcelos P, Ma CQ, Deng XD, de Souza ZS, Zhao YX, Wu G (2008) Origin of the Tongshankou porphyry-skarn Cu-Mo deposit, eastern Yangtze craton, eastern China: geochronological, geochemical, and Sr-Nd-Hf isotopic constraints. Mineral Deposita 43:315–336

Lin L, Yu ZZ, Luo XH, Ding SH (2006) The metallogenic prognosis of Dahutang tungsten ore field in Jiangxi. J East China Inst Technol 3(s1):139–142 **(in Chinese)**

Lin L, Zhang GL, Yu XP (2006) Geological characteristics and ore-search prospect of Dahutang tungsten (tin) ore field in Jiangxi. Resour Surv Environ 27:25–28 **(in Chinese with English abstract)**

Ling MX, Wang FY, Ding X, Hu YH, Zhou JB, Zartman RE, Yang XY, Sun W (2009) Cretaceous ridge subduction along the lower Yangtze River belt, eastern China. Econ Geol 104:303–321

Liu YS, Hu ZC, Gao S, Günther D, Xu J, Gao CG, Chen HH (2008) In situ analysis of major and trace elements of anhydrous minerals by LA-ICP-MS without applying an internal standard. Chem Geol 257: 34–43

Mao JW, Cheng YB, Chen MH, Pirajno F (2013) Major types and time–space distribution of Mesozoic ore deposits in South China and their geodynamic settings. Mineral Deposita 48:267–294

Mao ZH, Cheng YB, Liu JJ, Yuan S, Wu S, Xiang X, Luo X (2013) Geology and molybdenite Re–Os age of the Dahutang granite-related veinlets-disseminated tungsten ore field in the Jiangxi Province, China. Ore Geol Rev 53:422–433

Mao ZH, Liu JJ, Mao JW, Deng J, Zhang F, Meng XY, Xiong BK, Xiang XK, Luo XH (2015) Geochronology and geochemistry of granitoids related to the giant Dahutang tungsten deposit, middle Yangtze River region, China: implications for petrogenesis, geodynamic setting, and mineralization. Gondwana Res 28:816–836

Mao JW, Xiong BK, Liu J et al (2017) Molybdenite Re/Os dating, zircon U–Pb age and geochemistry of granitoids in the Yangchuling porphyry W–Mo deposit (Jiangnan tungsten ore belt), China: implications for petrogenesis, mineralization and geodynamic setting. Ore Geol Rev 286-287:35–52

Nabelek PI, O'Neil JR, Papike JJ (1983) Vapor phase exsolution as a controlling factor in hydrogen isotope variation in granitic rocks: the Notch Peak granitic stock, Utah. Earth Planet Sci Lett 66:137–150

Ohmoto H (1972) Systematics of sulfur and carbon isotopes in hydrothermal ore deposits. Econ Geol 67:551–578

Pan XF, Hou ZQ, Li Y, Chen G, Zhao M, Zhang T, Zhang C, Wei J, Kang C (2017) Dating the giant Zhuxi W–Cu deposit (Taqian–Fuchun Ore Belt) in South China using molybdenite Re–Os and muscovite Ar–Ar system. Ore Geol Rev 86:719–733

Polya DA, Foxford KA, Stuart F, Boyce A, Fallick AE (2000) Evolution and paragenetic context of low δD hydrothermal fluids from the Panasqueira W-Sn deposit, Portugal: new evidence from microthermometric, stable isotope, noble gas and halogen analyses of primary fluid inclusions. Geochim Cosmochim Acta 64:3357–3371

Rajabpour S, Behzadi M, Jiang SY, Rasa I, Lehmann B, Ma Y (2017) Sulfide chemistry and sulfur isotope characteristics of the Cenozoic volcanic-hosted Kuh-Pang copper deposit, Saveh county, northwestern central Iran. Ore Geol Rev 86:563–583

Roedder E (1979) Origin and significance of magmatic inclusions. Bull Mineral 102:487–510

Roedder E (1992) Fluid inclusion evidence for immiscibility in magmatic differentiation. Geochim Cosmochim Acta 56:5–20

Rye RO, Ohmoto H (1974) Sulfur and carbon isotopes and ore genesis: a review. Econ Geol 69:826–842

Shinohara H (1994) Exsolution of immiscible vapor and liquid phases from a crystallizing silicate melt: implications for chlorine and metal transport. Geochim Cosmochim Acta 58:5215–5221

Soloviev SG, Kryazhev SG (2017) Geology, mineralization, and fluid inclusion characteristics of the Skrytoe reduced-type W skarn and stockwork deposit, Sikhote-Alin, Russia. Mineral Deposita 52:1–26

Student JJ, Bodnar RJ (2004) Silicate melt inclusions in porphyry copper deposits: identification and homogenization behavior. Can Miner 42:1583–1599

Sun SS, McDonough WF (1989) Chemical and isotopic systematics of oceanic basalts: implications for mantle composition and processes. In: Saunders AD, Norry MJ (eds), Magmatism in the Ocean Basins. Geol Soc Spec Publ 42, pp 313–345

Veksler IV (2004) Liquid immiscibility and its role at the magmatic-hydrothermal transition: a summary of experimental studies. Chem Geol 210:7–31

Wagner T, Mlynarczyk MSJ, Williams-Jones AE, Boyce AJ (2009) Stable isotope constraints on ore formation at the San Rafael tin-copper deposit, Southeast Peru. Econ Geol 104:223–248

Wang H, Feng CY, Li DX, Xiang XK, Zhou JH (2015) Sources of granitoids and ore-forming materials of Dahutang tungsten deposit in northern Jiangxi Province: constraints from mineralogy and isotopic tracing. Acta Petrol Sin 31:725–739 **(in Chinese with English abstract)**

Webster JD (2004) The exsolution of magmatic hypersaline chloride liquids. Chem Geol 210:33–48

Webster JD, Thomas R (2006) Silicate melt inclusions in felsic plutons: a synthesis and review. In: Webster JD (ed), Melt Inclusions in Plutonic Rocks. Miner Assoc Canada Short Course Ser 36, pp 165–188

Xiang XK, Fang P, Zhan GN et al (2013) Geological characteristics of Shimensi tungsten polymetallic deposit in northern Jiangxi Province. Mineral Deposits 32:1171–1187 **(in Chinese with English abstract)**

Xiang XK, Liu XM, Zhan GN (2012) Discovery of Shimensi super-large tungsten deposit and its prospecting significance in Dahutang area, Jiangxi Province. Resour Surv Environ 33:141–151 **(in Chinese with English abstract)**

Xiang XK, Wang P, Sun DM, Zhong B (2013) Isotopic geochemical characteristics of the Shimensi tungsten-polymetallic deposit in northern Jiangxi province. Acta Geosci Sin 34:263–271 **(in Chinese with English abstract)**

Xie GQ, Mao JW, Zhao HJ, Cao D, Yao L (2012) Zircon U-Pb and phlogopite ^{40}Ar-^{39}Ar age of the Chengchao and Jinshandian skarn Fe deposits, southeast Hubei Province, middle-lower Yangtze River valley metallogenic belt, China. Mineral Deposita 47:633–652

Ye ZH, Wang P, Xiang XK, Yan Q, Li YK, Guo JH (2017) Early cretaceous tungsten mineralization in southeastern China: the Wuning example. Int Geol Rev 59:946–964

Zartman RE, Doe BR (1981) Plumbotectonics—the model. Tectonophysics 75:135–162

Zhao WW, Zhou MF, Martin Li YH, Zhao Z, Gao JF (2017) Genetic types, mineralization styles, and geodynamic settings of Mesozoic tungsten deposits in South China. J Asian Earth Sci 137:109–140

Zheng J, Griffin WL, O'Reilly SY, Zhang M, Pearson N, Pan Y (2006) Widespread Archean basement beneath the Yangtze craton. Geology 34:417–420

Zhou XM, Sun T, Shen WZ, Shu LS, Niu YL (2006) Petrogenesis of Mesozoic granitoids and volcanic rocks in South China: a response to tectonic evolution. Episodes 29:26–33

Zhu ZY, Jiang SY, Ciobanu CL, Yang T, Cook NJ (2017) Sulfur isotope fractionation in pyrite during laser ablation: implications for laser ablation multiple collector inductively coupled plasma mass spectrometry mapping. Chem Geol 450:223–234